



HAL
open science

On the optimal window size in optical flow and cross-correlation in particle image velocimetry: application to turbulent flows

Antonios Giannopoulos, Pierre-Yves Passaggia, Nicolas Mazellier, Jean-Luc Aider

► To cite this version:

Antonios Giannopoulos, Pierre-Yves Passaggia, Nicolas Mazellier, Jean-Luc Aider. On the optimal window size in optical flow and cross-correlation in particle image velocimetry: application to turbulent flows. *Experiments in Fluids*, 2022, 63 (3), pp.57. 10.1007/s00348-022-03410-z . hal-03848429

HAL Id: hal-03848429

<https://hal.science/hal-03848429>

Submitted on 17 Nov 2022

HAL is a multi-disciplinary open access archive for the deposit and dissemination of scientific research documents, whether they are published or not. The documents may come from teaching and research institutions in France or abroad, or from public or private research centers.

L'archive ouverte pluridisciplinaire **HAL**, est destinée au dépôt et à la diffusion de documents scientifiques de niveau recherche, publiés ou non, émanant des établissements d'enseignement et de recherche français ou étrangers, des laboratoires publics ou privés.

1 **On the optimal window size in optical flow and**
2 **cross-correlation in particle image velocimetry:**
3 **Application to turbulent flows**

4 **Antonios Giannopoulos¹ · Pierre-Yves Passaggia² ·**
5 **Nicolas Mazellier³ · Jean-Luc Aider⁴.**

6
7 November 17, 2022

8 **Abstract** Two Particle Image Velocimetry (PIV) softwares applied to turbulent flows are
9 compared. One is based on a standard Cross-Correlation (CC) algorithm and the other is
10 based on an iterative multi-pyramid Optical Flow (OF) algorithm. First, still particle images
11 are used to evaluate the cut-off frequency induced by each method. Then a step response
12 analysis highlights the capabilities of each method to minimise the effect of unresolved
13 velocity gradients. Two different benchmarks with various turbulent length-scales, down to
14 the Taylor micro-scale, are then used to analyse the velocity spectra and the turbulent kinetic
15 energy dissipation estimation. First, a synthetic PIV dataset of homogeneous isotropic tur-
16 bulance is processed and compared with Direct Numerical Simulation (DNS) results. Then
17 a grid turbulence wind tunnel experimental dataset is used to calculate velocity spectra and
18 second-order structure functions, which are compared to Laser Doppler Velocimetry spectra.
19 All these results point to the fact that, although OF is more diffusive and up to 5% less accu-
20 rate than cross correlation, the numerical diffusion improves the calculation of sub-window
21 unresolved gradients and allows for direct and more robust measurement of the onset of the
22 viscous subrange in experimental turbulent flows.

23 **Keywords** Particle Image Velocimetry, Optical Flow, Cross-Correlation, turbulence
24 spectrum.

¹Laboratoire de Physique et Mécanique des Milieux Hétérogènes (PMMH), UMR7636 CNRS, ESPCI Paris, PSL Research University, Sorbonne Université, Univ. Paris Diderot, 1 rue Jussieu, 75005 Paris, France.

E-mail: antonios.giannopoulos@espci.fr · Also affiliated: Photon Lines, Parc Pereire Bât B, 99 rue Pereire, 78100 – Saint-Germain-en-Laye, France

²University of Orléans, INSA-CVL, PRISME, EA 4229, 45072, Orléans, France E-mail: pierre-yves.passaggia@univ-orleans.fr · Also affiliated: Carolina Center for Interdisciplinary Applied Mathematics, Dept. of Mathematics, University of North Carolina, Chapel Hill, NC 27599, USA

³University of Orléans, INSA-CVL, PRISME, EA 4229, 45072, Orléans, France E-mail: nicolas.mazellier@univ-orleans.fr

⁴Laboratoire de Physique et Mécanique des Milieux hétérogènes (PMMH), UMR7636 CNRS, ESPCI Paris, PSL Research University, Sorbonne Université, Univ. Paris Diderot, 1 rue Jussieu, 75005 Paris, France E-mail: jean-luc.aider@espci.psl.eu.

1 Introduction

Particle Image Velocimetry (PIV) has been widely used for almost 40 years in fluid dynamics research and the industry. It carries a long history of techniques which have gradually improved over the years [53,36,39]. Digital PIV (DPIV) uses two successive particle images that record the displacement of particles over a dozen pixels. This method has been used extensively and led to different correlation methods in order to obtain an instantaneous 2-Dimensional 2-Components (2D2C) velocity field from two snapshots. At this point, two methods stand out. On one hand, Particle Tracking Velocimetry (PTV) is traditionally used to analyse particle tracks from series of particle images where the tracks are used to obtain the velocity and acceleration from sparse particles in a Lagrangian frame. On the other hand, PIV uses Cross Correlation (CC) to determine the mean displacement of particles from a correlation window, based on a couple or more instantaneous particle images of the flow. PIV gives results in an Eulerian frame, so a direct comparison with PTV is not possible unless a coordinate system conversion is performed from Lagrangian to the Eulerian frame for direct comparison. While this approach is widely used in experimental fluid dynamics, different algorithms have been developed in order to calculate the correlation between two successive frames.

Most CC-based algorithms are based on Fast Fourier Transform (FFT) to calculate the CC more efficiently than direct correlation. Such algorithms have been extensively used across the literature and have been adapted to a large range of flows. Despite its efficiency and high accuracy, FFT-based cross-correlation algorithms present a few drawbacks including peak locking [53], and unresolved velocity gradient [27]. Various CC PIV algorithms were compared for various data-sets during the four PIV challenges [43–45,20]. We use part of these data-sets in the present study.

In addition, it has been shown that overlapping the correlation boxes beyond 50% did not improve the quality of the correlation, nor the accuracy of the gradients [8]. It only leads to oversampling of the velocity field without any gain in accuracy. In fact, the cut-off frequency is only dependent on the size of the correlation box and remains constant for spatial frequencies lower than 2.8 divided by the size of the correlation box. This bound is extremely important, and shows that in order to improve the accuracy of CC-based algorithms, one may either use very large particle images with a very dense seeding, or design a fast algorithm that can perform equivalently than direct correlation which does not suffer the curse of the box size (i.e. the length of the correlation window). The same group [15] recently showed that when PIV is used to measure turbulence, it can be treated as a time-dependent signal and hence the noise between different realisations and different interrogation volumes is statistically independent.

Optical Flow (OF) algorithms, first introduced in machine vision by Horn & Shunck [18], provides an interesting alternative. Their first applications to PIV followed years later [31,34] and since have been increasingly used in fluid laboratory experiments.

Even if OF algorithms lead to dense velocity fields (one vector per pixel), it seems that their spatial resolution was no better than standard cross-correlation Fast-Fourier Transform (FFT) PIV algorithms, although ranked among the top 5 for various benchmarking tests [43,44]. Recently, Seong *et al.* [40] showed that OF can also be used to improve cross-correlation PIV results.

Turbulent data-sets are excellent test cases to compare PIV algorithms: they contain high gradients, large velocity differences inside the same field and are governed by universal laws for their relative spectra. Hence, they can be used as benchmarks leading to a better understanding of the advantages and disadvantages of each algorithm.

73 Very recently, machine learning algorithms have been also tested to perform PIV with
74 promising expectations for the future of the community [32,7,2]. Moreover, [38,37] pro-
75 posed a wavelet-based OF method to improve the resolution and accuracy of standard Cross-
76 Correlation PIV, and in particular, the estimation of the planar velocity vector field, which
77 is somewhat close to windowing the correlation box but provides more flexibility on the
78 sample size.

79 To this date though, very few studies compare the accuracy of OF, Direct-Cross-Correlation,
80 and FFT-based CC [21,23,5]. This is the objective of the present study.

81 In this paper, we begin with the same ideas than Foucaut *et al.* [8] and analyse still
82 particle images to understand how band-pass filtering compares between OF and CC. The
83 analysis is extended to the step response analysis to understand how unresolved velocity gra-
84 dients affect both CC and OF. In particular, we extend the framework developed in [19] and
85 analyse the statistics (mean and variance) of the step response. We are therefore able to draw
86 a clearer picture on the advantages and disadvantages of each method when applied to either
87 laminar or turbulent flows. Then, we analyse a two-dimensional turbulence data-set gener-
88 ated from a Direct Numerical Simulation (DNS) without noise to evaluate the performance
89 of each approach to compute the spectrum in the deep viscous regime. The results are then
90 compared to the DNS data. Finally, we consider one experimental test case: the turbulent
91 flow downstream a regular grid. Our results show on both test cases that CC is outperformed
92 by OF when attempting to directly measure the viscous sub-range. These results reveal that
93 when considering turbulent flows, OF is well adapted to their analysis and more appropriate
94 than CC. Instead, CC seems to provide a more accurate alternative when analysing laminar
95 flows or when velocity gradients are well resolved by the interrogation window.

96 2 Cross-Correlation and Optical Flow applied to PIV

97 2.1 Cross-correlation based PIV

98 This section presents the measurement strategy for the cross-correlation algorithm which
99 was originally developed by Meunier & Leweke (DPIVSoft) [27], who analysed errors gen-
100 erated by two-dimensional CC PIV algorithms (with window shifting), when large velocity
101 gradients are present. A sketch of the cross-correlation procedure is depicted in Fig. 1.

102 The algorithm first re-estimates the correlation function by raising its values far from
103 the centre. This is due to the in-plane loss of pairs in the case of FFT calculation (see [33]).
104 The correlation function is thus recalculated around its maximum and the algorithm then fits
105 the peak and its neighbours by a Gaussian function.

106 In classical CC-based PIV, a first bias error is due to the difference between the La-
107 grangian displacement of a particle and the real velocity. This error has been calculated
108 theoretically as a function of the velocity gradients, and is shown to reach values up to 1
109 pixel if only one window is translated [27]. However, it becomes negligible when both win-
110 dows are shifted in a symmetric way. Meunier & Leweke also showed that a second error
111 source is linked to the image pattern deformation, which decreases the height of the corre-
112 lation peaks. In order to reduce this effect, the windows in DPIVSoft [27,30,3,29,41] are
113 deformed according to the velocity gradients in an iterative process. The problem of finding
114 a sufficiently reliable starting point for the iteration is solved by applying a Gaussian filter
115 to the images for the first correlation. The approach of Meunier & Leweke implemented
116 in DPIVSoft thereby minimizes the displacement error in an iterative manner, finding the

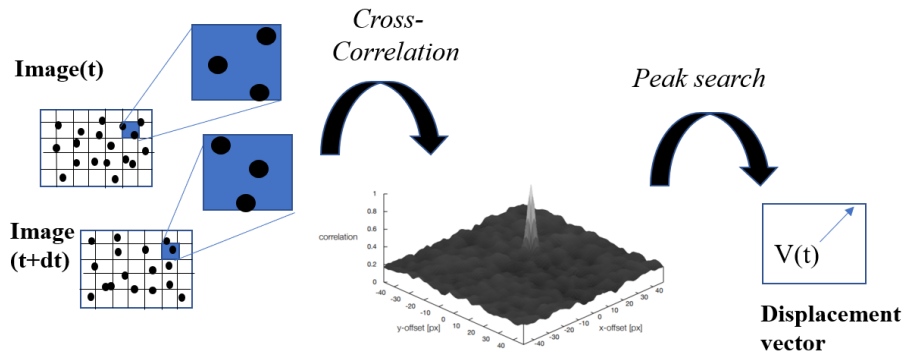


Fig. 1: Sketch of the CC-PIV process using cross-correlation and peak-search to estimate velocity vectors from a couple of successive images.

117 optimal displacement and deformation for the correlation box. The results were found to
 118 recover the same accuracy than commercial software for still and moving particle images.

119 The size of the correlation box is set by different parameters such as the particle size,
 120 particle density, and particle displacement [19]. In this study, we analyse the effect of the
 121 box size with dimensions increasing in powers of 2. Thereby, squares boxes with sizes 16,
 122 32, and 64 pix^2 were considered. The mean displacement for each experiment was found to
 123 be approximately 4 pix for the HIT (Homogeneous Isotropic Turbulence) dataset and 8 pix
 124 for the grid-turbulence experiment. For all experiments, the mean diameter of the particles
 125 was approximately two or three pixels.

126 The FFT-based CC implemented in DPIVSoft is also performed in an iterative way over
 127 successive passes such that each iteration is performed not only once but iterated several
 128 times in order to converge towards optimal box displacements and optimal box shape mod-
 129 ification. Hence, at the end of each iteration, the displacement vector is stored and used as
 130 an update for the shapes and displacement of the correlation window. In practice, no more
 131 than 5 iterations were necessary for correlations to converge in each window.

132 The second part of the iterative scheme deals with pyramid levels which are imple-
 133 mented in DPIVSoft using a multigrid approach. At first, boxes with size $4X$ (where X is the
 134 final size of the correlation box) are used for the cross-correlation and iterated as discussed
 135 previously. Then, a second grid is considered which is twice smaller than the original grid
 136 (i.e. with size $2X$) and therefore gives rise to four times more vectors. An additional level is
 137 then computed to reach the final box size X with up to 5 sub-iterations in order to obtain the
 138 final velocity field.

139 The next section addresses the Optical Flow method. We will show later that both meth-
 140 ods present different accuracy and robustness to unresolved measurements.

141 2.2 Optical Flow for PIV

142 A variational OF method was first proposed by Horn and Schunck [18] to solve motion
 143 estimation problems. The estimation relied on finding the optimal displacement field $[u, v]$
 144 to achieve the energy minimisation of an objective function which consists of an intensity

145 energy term (based on brightness conservation assumption) and a regularisation energy term.
146 Although firstly introduced in the field of machine vision, OF methods have been applied
147 in the field of fluid mechanics as well. Various OF algorithms were benchmarked multiple
148 times during the four international PIV challenges [43–45,20]. Most of them were found of
149 equivalent precision and spatial resolution compared to CC PIV algorithms for most of the
150 challenges. Even a 3D PIV OF algorithm was benchmarked [20], ranking amongst the top 5
151 competitors.

152 An hybrid CC-OF PIV method was also presented by [23]. Furthermore, [52] used a
153 multi-pyramid-type scheme optimisation algorithm (used traditionally in OF) in order to
154 globally minimise an objective function consisting of a CC term, a penalty term for smooth-
155 ness and an empirical smoothing parameter. They thus obtained superior resolution results
156 compared to standard CC PIV and outperforming OF for small vortex resolution, but losing
157 compared to OF for error analysis in particle concentration, particle image diameter, large
158 displacements and image noise. CC PIV and OF have also been used for biological image
159 data-sets [51]. OF showed clear advantages to extract additional biophysical / chemical in-
160 formations such as local vorticity or net polymerisation rates from speckle microscopy. Last
161 but not least, OF algorithms have been also applied in experimental machine learning flow
162 control experiments [14] as well as System Identification studies with quite satisfying results
163 [17,16,13].

164 In the present study we benchmark a dense, multi-pyramid, iterative Lucas-Kanade OF
165 algorithm. The first version of the code has been developed at ONERA [5] and later modi-
166 fied, optimised and adapted to the constraints of real-time measurements by Gautier & Aider
167 [13] to allow closed-loop flow control experiments based on data extracted in real-time from
168 the "visual sensor" [12]. The advantage of this algorithm, compared to a standard FFT-PIV
169 algorithm, is its high computational speed when implemented with CUDA functions on a
170 GPU (Graphics Processor Unit). OF processing time is approximately 50 times faster than
171 state-of-the-art CC-PIV software [28,5].

172 The basic principle is different from CC-PIV. It consists in estimating at each pixel m the
173 intensity displacement which minimises the sum of square differences between the intensity
174 over a warped Interrogation Window (IW), of size equal to the Kernel Radius (KR) at time t
175 and the intensity over the warped IW at the successive time $t' = t + dt$. A synthetic PIV data-
176 set was used by [28] to benchmark the spatial resolution, which was found equivalent to the
177 CC PIV competitors. This algorithm was used by [6,35] to quickly post-process their PIV
178 snapshots for a turbulent jet flow study and for an investigation of the interaction between a
179 shock wave and a turbulent boundary layer, respectively. OF has been used numerous times
180 for time-resolved and real-time PIV measurements. The high spatial resolution together with
181 the low computational time proved useful in various physics experiments [50] as well as for
182 flow control experiments [11,10,12,49]. Another comparison [22] showed superior spatial
183 resolution for OF compared to CC PIV.

184 The Kernel Radius (KR), defined in pixels, is the size of the IW centred around each
185 pixel, as seen in Fig. 2. Larger KR values yield smoothed-convoluted results, that are on
186 the other hand more robust to noise and particle density variations. Smaller KR values may
187 increase the spatial resolution but also measurement noise. Note that it plays a secondary
188 role in the computational time.

189 Multi-pyramid computational schemes are standard algorithms widely used in computa-
190 tions. They provide a better initial condition estimation for the iterative scheme and increase
191 drastically the number of maximum possible particle displacement. At each pyramid level,
192 the upper level is obtained by applying a low-pass filter, hence down-sampling the image
193 size by a factor of 2 in each direction, as shown in Fig. 2. In the present algorithm, a Burt-

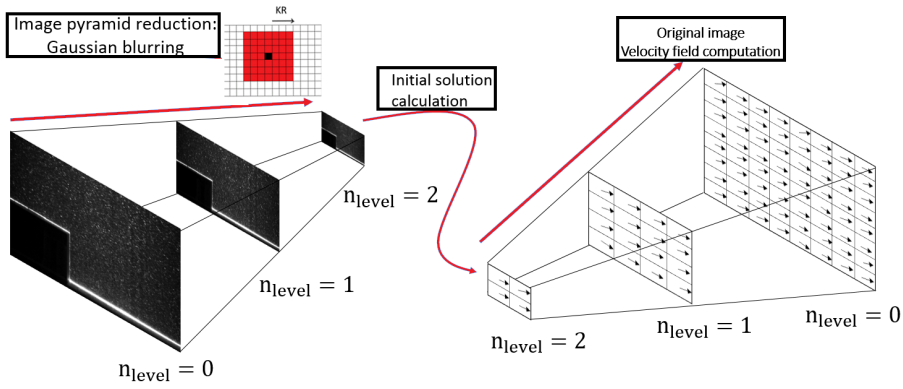


Fig. 2: Illustration of a typical OF pyramid reduction scheme using 3 levels, and KR definition, used for Gaussian blurring in the pixel neighbourhood of size $(2 \times KR + 1)^2$.

194 Adelson pyramid [1] is implemented. This specific parameter was introduced so that more
 195 than 2 pixels displacements can be calculated, which is a typical problem of initial OF algo-
 196 rithms [18]. With the increase of pyramid levels there is no upper limit on the maximum
 197 displacement that can be calculated. Practically though, for standard PIV image data-sets,
 198 one can rarely observe a non-fictitious displacement of more than 20 pixels.

199 3 Comparison of the filtering effect of Optical Flow and Cross Correlation

200 3.1 Steady particle images: noise response analysis

201 A single experimental snapshot of still particles was used to study the filtering effect of each
 202 algorithm. The data-set corresponds to neutrally buoyant PIV particles from CosphehicTM,
 203 at rest in a stratified salt water tank [29]. The average particle image diameter is 3 px while
 204 the mean particle concentration is 0.01 ppp, with the particle concentration measured in
 205 Particles Per Pixels (ppp) and defined as:

$$C_p = N / (n_x n_y) \quad (1)$$

206 where N is the number of particles in the control box, while n_x and n_y are the sizes of
 207 the control box in the two directions. In the following, we will consider sizes of IW and KR
 208 as power of 2 (16, 32 and 64 pixels), which are standard values, but one has to keep in mind
 209 that both algorithms work with any integer values.

Window size / Method	Number of fields	Mean disp. along x (pix)	Mean disp. along y (pix)	Std dev. σ_u (pix)	Std dev. σ_v (pix)
16 × 16 CC	1	0.010	0.0029	0.985	0.212
32 × 32 CC	1	0.009	0.0019	0.439	0.092
64 × 64 CC	1	0.008	0.0016	0.280	0.048
16 × 16 OF	1	0.008	0.007	0.185	0.148
32 × 32 OF	1	0.007	0.003	0.114	0.071
64 × 64 OF	1	0.006	0.002	0.056	0.044

Table 1: Systematic and random errors on the two components of the velocity field computed from no-motion snapshots with CC-PIV and OF.

Particle images can be considered as a two-dimensional discretized signal where particles are sampled over few pixels. Assuming that the displacement of the particles is close to null, there only remains the noise from the camera and from the experimental setup such as the misalignment of the laser or optical aberrations, to only cite a few. Following [8], we proceed with a spectral analysis and compare how both CC and OF respond to nearly-zero-displacement images. In particular, we adapt their analysis and assume that the IW used in both methods can be modelled by the convolution of the particle image sample with a square window, whose Fourier transform corresponds to a multiplication by a *sinc* function in the spectral domain. As suggested by [24], the power spectra of the noise for no-motion particle images can be expressed as:

$$E_{ii} = E_{noise} \left(\frac{\sin(kX/2)}{kX/2} \right)^2, \quad (2)$$

where E_{noise} is the white-noise level introduced by measurement errors. In the present study, E_{noise} corresponds to the intercept at the smallest wave numbers of the spectrum measured from OF and CC, which is assumed to have the form given by Eq. (2).

The results are compared in Fig. 3(a) and Fig. 3(b) for CC, and Fig. 3(c) and Fig. 3(d) for OF. Note that the spectra has been rescaled with the interrogation window size X or Y for CC and with the kernel radius KR for OF. If $KR = X = Y = 32$, the noise amplitude is $E_{noise} = 9 \times 10^{-3} \text{ pix}^3$ and $1.9 \times 10^{-3} \text{ pix}^3$ respectively for E_{11} and E_{22} for CC and $E_{noise} = 7 \times 10^{-3} \text{ pix}^3$ and $3 \times 10^{-3} \text{ pix}^3$ respectively for E_{11} and E_{22} in the case of OF. It is interesting to note that in the vertical direction, CC provides about twice less mean displacement than OF.

First, the noise level for E_{22} is essentially the same for both CC and OF, in agreement with the values of the standard deviation in Tab. 1. The main difference is observed for E_{11} which is the direction along which the CCD camera transfers data. In this direction, it has already been noted that E_{11} was much larger than E_{22} for a similar PIV equipment [8]. We also obtain a ratio $E_{11}/E_{22} \approx [2 - 5]$ close to the one reported in [8] in the case of CC. This is to be expected since the data transfer in the x direction introduces noise which will be detected by the cross correlation.

The noise level for OF is equivalent between E_{11} and E_{22} because of the way the correlation is computed. OF averages the square of the intensity over the interrogation window, which is equivalent to a mean energy. The noise within the interrogation window is therefore averaged and turns out to be close to zero for a white noise. Thus, OF is expected to be less sensitive to white noise than CC, which explains the difference for E_{11} between both methods. This should not be a problem for CMOS sensors.

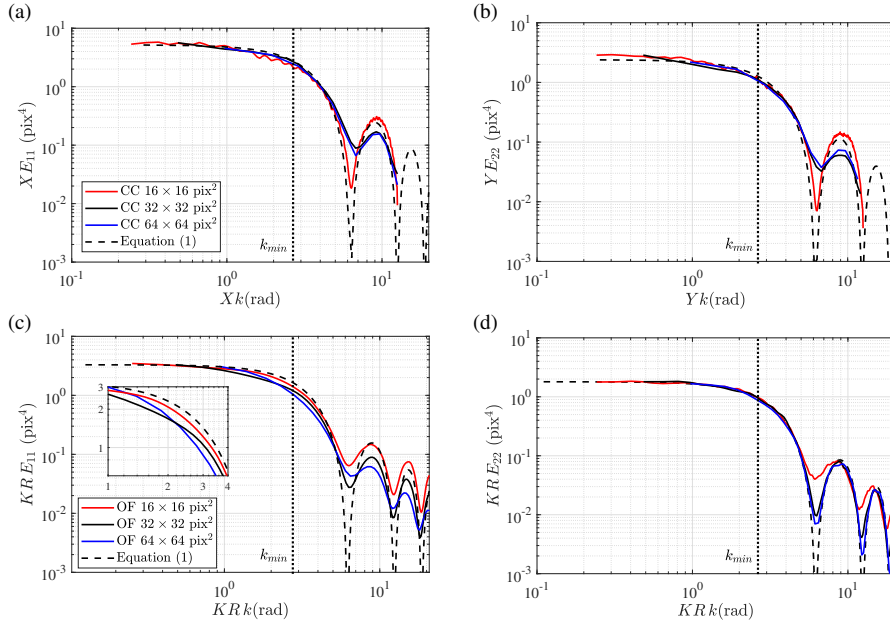


Fig. 3: Power spectra of displacements from no-motion PIV maps obtained with Cross-Correlation (with 75% overlap for CC) in (a) and (b) and Optical Flow (with an overlap of $(KR - 1)/KR > 93\%$) in (c) and (d), along the x direction in (a) and (c) and along the y direction in (b) and (d).

245 The error between the horizontal and the vertical components of the displacement in-
 246 duced by the noise are reported in Tab. 1 and varies differently for OF and CC. Cross cor-
 247 relation provides systematically smaller mean displacements than OF in the vertical direction.
 248 However, there is a substantial difference regarding the standard deviation: OF is weakly
 249 dependent on the vertical or horizontal direction while CC is much more sensitive and dif-
 250 ferences are much larger depending on the direction. This result hints to the idea that OF
 251 is less sensible to noise but also less precise than CC for small displacements in practical
 252 applications. In the following, the results presented correspond to E_{22} and are generalised to
 253 E_{ii} .

254 The cutoff frequency produced by each PIV method can be seen as the decrease by
 255 -3dB between the E_{ii} measured at the intercept (i.e. $k = 0$). This cutoff corresponds to
 256 the lower significant wavenumber for which the velocity is not filtered by the interrogation
 257 window size. As shown by the theoretical expression in Eq. (2), the *sinc* function is the
 258 standard low-pass filter introduced by the square window whose cutoff wavenumber gives
 259 $k_{min} = 2.8 \text{ rad/pix}$ for CC and $k_{min} = [1.34 - 2.7] \text{ rad/pix}$ for OF in the horizontal direction
 260 and $k_{min} = 2.8 \text{ rad/pix}$ in the vertical direction. Note that this value may actually increase
 261 up to $k_{min} = 2.8$ when decreasing the KR size, as shown in the inset in Fig. 3(c). This
 262 value is shown in Fig. 3(a-d) by a vertical dashed line. OF may therefore be considered
 263 more diffusive than CC when the kernel radius size is larger than 16 px and it is therefore
 264 necessary to use an interrogation window twice smaller in the worst case for OF than CC
 265 for $KR > 16$ to obtain results with similar cutoff frequencies. Note that the vertical spectrum
 266 is not affected at all. In the following, an overlapping of 75% for CC will be used in order

267 to detect easily the *sinc* function, although an overlap larger than 50% is not necessary in
 268 practice [8].

Window sizes	ζ_1 (px ⁴)	ζ_2 (px ⁴)	σ_u estimated	σ_v estimated
16 × 16 CC	8.4	2.08	0.857	0.214
32 × 32 CC	8.1	1.99	0.432	0.105
64 × 64 CC	7.9	1.92	0.212	0.050
16 × 16 OF	2.15	1.40	0.208	0.176
32 × 32 OF	1.86	1.39	0.099	0.085
64 × 64 OF	1.72	1.38	0.048	0.042

269 Table 2: Spectral noise density and estimated standard deviations of noise for both methods
 270 and various window sizes.

271 For OF, the overlap is given by $(KR - 1)/KR$, which is close to 100% overlap (a vec-
 272 tor is computed on each pixel). It is interesting to note that OF produces exactly the same
 273 windowing-type filter on the spectra shown in Fig. 3(b) and Fig. 3(d). The dense approach to
 274 the Lucas-Kanade algorithm can therefore be subsampled or binned down to near wavenum-
 275 bers with values of $2KR$ rad/px in the horizontal direction when noise is present. The vertical
 276 spectrum seems not to be affected at all.

277 As a first step, an approach based on spectral computations varying the window size
 278 X or the KR was carried out. This study shows that the cut-off frequency computed from
 279 $k_c X = k_c Y = 2.8$ remains universal for CC [8]. This is also the case for OF where the value
 280 remains essentially constant to nearly 2.8 for $KR < 16$ (see Fig. 3(d)). However, this is not
 281 the case for OF where the cut-off wavenumber decreases to $k_c KR = 2$ for $KR = 64$ which is
 282 nearly 50% lower than what is found for CC. This value increases to nearly 2.8 for $KR = 16$
 283 (see Fig. 3(c)). In other words, OF is more diffusive and slightly less precise than CC, both
 284 in noise amplitude (Tab. 2) and the cut-off frequency when noise is present. We will retain
 285 these values as references hereinafter. Note that if this decrease in wavenumber cutoff can
 286 first appear as a weakness in the algorithm, it will later prove to introduce a numerical-type
 287 diffusion which will become important when considering unresolved velocity gradients and
 288 thus, turbulent flows applications.

289 In what follows, the representation of the spectra is rescaled by the window size X such
 290 that $E_{ii} = E_{ii}(kX)$ for CC and equivalently using KR for OF which remains universal, in-
 291 dependently of the method. The noise level for CC is constant at a value of approximately
 292 $8px^4$, while we obtain $1.9px^4$ for OF in the horizontal direction. The vertical direction pro-
 293 vides similar results for both methods.

294 Then, we compute both spectra varying $Y = X$. The E_{noise} values for the horizontal
 295 directions are 0.525, 0.231 and 0.123 px^4 respectively for $Y = X = 16, 32$ and 64 pixels for
 296 CC. The E_{noise} values are 0.134, 0.058 and 0.026 px^4 respectively for $KR = 16, 32$ and 64
 297 pixels for OF.

298 As noted in [8], E_{noise} varies with the inverse of Y and the data can be represented
 299 as $YE_{ii}(kY)$. Rescaling the wavenumbers with Y and multiplying the left-hand side by the
 300 interrogation window size Y , eq. (2) becomes:

$$YE_{ii} = \zeta \left(\frac{\sin(kY)}{kY} \right)^2. \quad (3)$$

301 Fig. 3(a) and (b) show these spectra for CC while OF is depicted in Fig. 3(c) and Fig. 3(d)
 302 computed for different window sizes (16, 32, and 64 pixels) for square interrogation win-
 303 dows with aspect ratios of 1.

The rescaled spectra given by Eq. (3) is shown in Fig. 3(a-d) alongside the rescaled no-motion spectra measured with CC and OF where a good agreement is obtained for both methods. Nevertheless $\zeta = E_{noise}Y$ remains essentially constant for all window size of kernel radii depending on the direction and takes a constant value of 8 px^4 for CC and 1.8 px^4 for OF in the case of the horizontal direction. This result confirms that the cut-off frequency obtained with OF due to the *sinc* function depends essentially on the window size X in the direction where the spectrum is computed. The noise level E_{noise} depends only on the IW size or the KR for CC and OF in a similar fashion.

As a conclusion, the best spectrum is obtained for both methods using a rectangular window with a small X to increase the cut-off frequency and a large Y to decrease E_{noise} which is equivalent to the conclusions obtained in [8].

The best compromise is thus to use square windows for CC or equivalently, a square kernel for OF. We therefore reach the same conclusion than in [8] where the standard deviation σ_u of the displacement decreases when the window size increases independently of the method. As shown in [8], σ_u is the square root of the integral of the power spectra and relates to the amplitude of the error. Based on eq. (3), σ_u can be directly obtained computing $\sigma_u = \sqrt{4\zeta I/(XY)}$, where $I = \int_0^{2\pi} (\sin(u)/u)^2 du = 1.492$ and $I = 1.418$ when using an overlap of 50%.

The values of ζ_1 and ζ_2 obtained from Fig. 3(b) and the estimations of σ_u and σ_v computed with eq. (3) are reported in Tab. 2 for the displacements along x and y respectively, using both CC and OF. It is worth emphasizing that the values of ζ_1 and ζ_2 are equivalent for OF and different for CC depending on the noise direction.

Although the interrogation window sizes or the kernel radii are different, the density ζ is nearly constant for a given direction. The small differences are probably due to an effect of convergence of the spectra or sub-sampling effects for CC. In Tab. 2 the estimated standard deviations compare favourably with the measured values given in Tab. 1.

3.2 Step-response analysis

To systematically determine the effective resolution for various interrogation windows and different algorithms, the resolution limit can be evaluated using a step-like velocity profile [19]. Such a profile may be seen as an infinitely thin shear layer or a very small eddy, given for instance by:

$$\Delta x(y) = \begin{cases} 5 \text{ px}, & y \geq 0 \\ 0 \text{ px}, & y < 0 \end{cases} \quad (4)$$

The step response is also frequently used in electrical engineering and control theory to analyse the transfer function associated with linear and nonlinear systems.

In the following, a synthetic PIV image generator provided by [47] has been used to create the particle images using the maximum particle diameter $d_\tau = 6 \text{ px}$ and the maximum particle concentration $C_p = 0.69 \text{ ppp}$ (see Fig. 4). The displacement is fixed at 5 pixels. The PIV image generator creates pairs of images illuminated by a laser sheet with a Gaussian light intensity distribution. The coordinates of the particles, as well as an out-of-plane motion are selected randomly [26]. The thickness of the laser sheet was given a value of approximately 34 pixels. It means that the out-of-plane distance includes the region where laser intensity is larger than I_0/e^2 , with $I_0 = 255$ the maximum intensity and $e = \exp(1)$ the

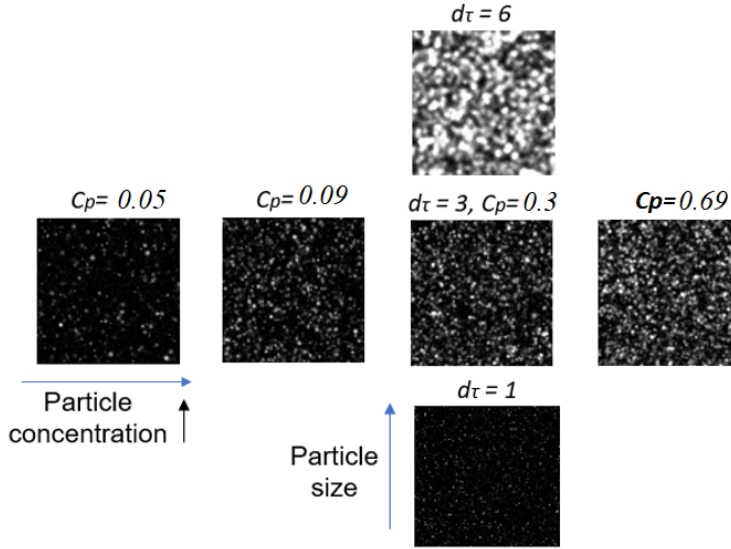


Fig. 4: Examples of synthetic particle images with increasing particle concentrations (from left to right) for a given particle diameter ($d_\tau = 3$ px) or with increasing particle diameters (from bottom to top) for a given concentration ($C_p = 0.3$ ppp). The size of the image is 100×100 px².

347 Euler number. Note that there is no out-of-plane motion between the two images since the
 348 same image is used for the first and second (i.e. sheared) image whose displacement is given
 349 by Eq. (4).

350

351 In order to analyse the accuracy of CC and OF, the signal (particle image displacement)
 352 is changed in space over an infinitely small distance. The response to the step profile is
 353 shown in Fig. 5(a,b) for three different IW sizes X for CC and four KR for OF. The Step
 354 Response Width (SRW) can be considered as the resolution and describes the minimum
 355 distance between independent vectors. Only for distances larger than the SRW, the vector is
 356 not biased by the aforementioned flow variations.

357 The sampling introduced by the window function, that is for both CC and OF can there-
 358 fore be regarded as a convolution between a step or Heaviside function with a square window
 359 function with a dimension KR for OF and Y for CC (since the shear is in the vertical direc-
 360 tion). The theoretical expression is a piecewise linear ramp of width KR (or equivalently Y)
 361 which is given by:

$$U(y) = \begin{cases} 0, & y < -KR/2, \\ \Delta x/KR \times Y - \Delta x/2, & -KR/2 \geq y \geq KR/2, \\ 1, & y > KR/2. \end{cases} \quad (5)$$

362 Note that local derivatives are computed using centred second-order finite differences sten-
 363 cils in the vertical direction and that both CC and OF gradients were evaluated on the same
 364 grids when $IW = KR$. It is worth highlighting that the gradient estimation could be further
 365 optimised using for instance least-squares estimation [9]. However, as noted in [9], centred

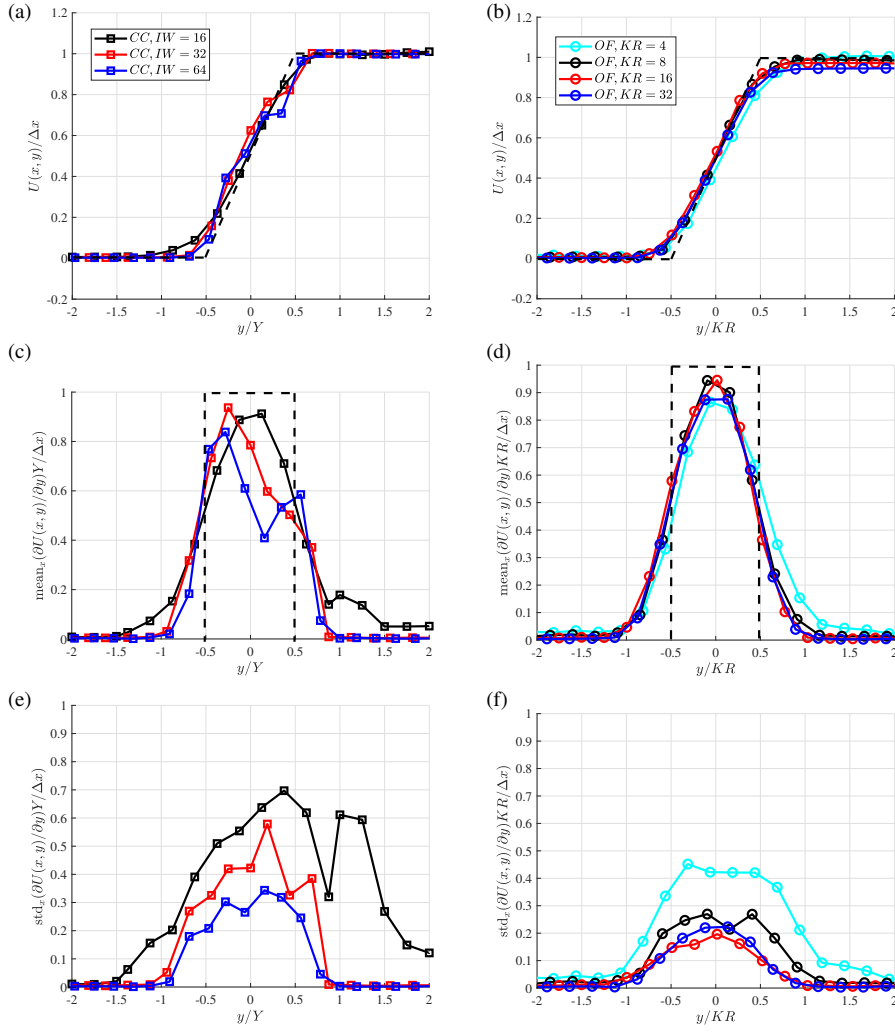


Fig. 5: Step-response analysis showing the mean normalised vertical profile of displacement $U(x,y)$ for (a) CC and (b) OF and for several interrogation windows and kernel sizes. Note that the horizontal axis is normalised using the interrogation window size of each method. Mean value of the vertical gradient of velocity computed along the horizontal direction x for CC (c) and OF (d). The theoretical profile is shown with black dashed lines in (a,b,c,d). Standard deviation of the vertical gradient along the spatial direction x for (e) CC and (f) OF. The particle diameter is $d_\tau = 3$ px and the particle concentration is $C_p = 0.69$ ppp.

366 second-order finite differences remains the best approximation when the window size is
 367 optimised for a particular flow for CC. As we will show later, derivatives obtained by OF
 368 behave differently and seem to be less sensitive to the window size used to compute velocity
 369 gradients.

370 We are interested in the velocity profile but also in its vertical derivative:

$$\frac{\partial U}{\partial y} = \begin{cases} 0, & y < -KR/2, \\ \Delta x/KR, & -KR/2 \geq y \geq KR/2, \\ 0, & y > KR/2. \end{cases} \quad (6)$$

371 In what follows, we analyse the Step Response Derivative Amplitude (SRDA) as well
 372 as its standard deviation for both CC and OF. Next, we determine how each method is able
 373 to resolve velocity gradients and the consequences when applied to turbulent flows. This
 374 aspect may shed light on how turbulent flows can be resolved using either OF or CC.

375
 376 The gradient is shown in Fig. 5(c,d) for both methods. The theoretical profile, given in
 377 Eq. (6) is clearly diffused since the normalised maximum for both CC and OF never reaches
 378 1 but is closer to 0.9. It translates into a diffusion effect of 10%, independently from the
 379 method used for the analysis.

380 It is interesting to see that the gradient obtained with CC is dependent on the size of the
 381 interrogation window and is not self-similar. As the IW size decreases, the mean gradient
 382 prediction improves and the derivative profile progressively steepens and approaches the
 383 theoretical profile when the size of the IW approaches 16 pixels.

384 The conclusion is somewhat different for OF. The mean derivative profiles remain self-
 385 similar, almost independently from the KR. Note that for $KR = 4$, the method is even more
 386 diffusive as the SRW is larger than for $KR > 4$. This aspect will be shown to have interesting
 387 implications for the analysis of turbulent spectra when applied to synthetic particle images
 388 of turbulence.

389 More interesting is the standard deviation of the gradients computed for the step re-
 390 sponse along the horizontal direction x , as shown in Fig. 5(e,f). This quantity relates the
 391 variance of the gradient, which is directly related to the notion of dissipation and hence,
 392 with the quality of the spatial gradient resolution. Ideally, each curve in Fig. 5(e,f) should
 393 be 0 along the y direction. However, the noise in the reconstruction inevitably leads to vari-
 394 ations, compared to the mean.

395 In the case of CC, the standard deviation decreases to a value of 0.3 for $X = Y = 64$ as
 396 the interrogation window increases. The case of OF is more interesting since the standard
 397 deviation peaks at 0.27 for $KR = 8$ and decreases to 0.2 for $KR = [16, 32]$. Therefore, the
 398 numerical diffusion induced by OF decreases the sensitivity to the step response, which can
 399 turn out to be particularly important for turbulent flows analyses. In fact, although more
 400 diffusive, OF may prove to be more robust in approximating the small scales in turbulent
 401 flows where the intrinsic filtering induces a numerical diffusion, which is less sensitive to
 402 particle size and concentration. This will be demonstrated in §5 on experimental data-sets.

403 As a general conclusion, OF is more diffusive than CC when calculating the step re-
 404 sponse to an infinitely thin shear layer but also more robust. In fact, Kernel radii with sizes
 405 $KR = 4$ and $KR = 8$ outperform results obtained with CC for interrogation windows with
 406 dimensions $X = 16$. Recalling from §3.1 that the cut-off frequency for OF is smaller than
 407 for CC, we can conclude that OF should allow for a better resolution of the vector fields
 408 with at least twice more vectors per direction.

409 Fig. 5(a,b) show the normalised step response for each method, for $d_\tau = 3$ px and $C_p =$
 410 0.69 ppp, which will serve as a reference case. From these figures, the normal direction is
 411 normalised with the IW size leading to the collapse of all curves on the theoretical profile
 412 given in Eq. (5).

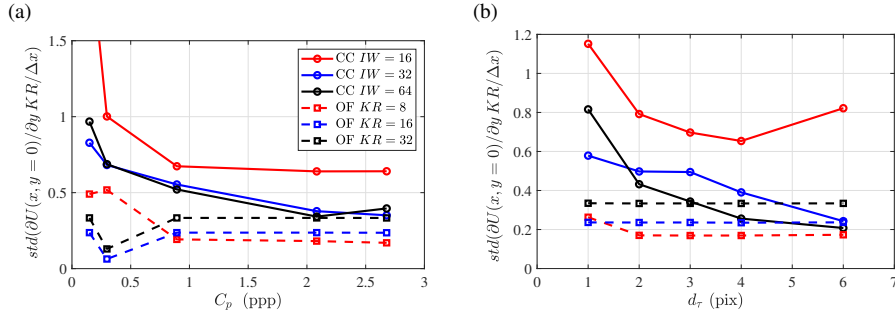


Fig. 6: Maximum of the standard deviation computed in Fig. 5(e,f) of the shear as a function of both (a) the particle concentration C_p computed for $d_\tau = 3$ px and (b) the actual particle size d_τ for $C_p = 0.69$ ppp. Here the continuous lines corresponds to the results obtained with CC while dashed line correspond to OF.

413 3.3 The effect of particle size and particle concentration

414 In what follows, we analyse the influence of the particle size d_τ and particle concentration
 415 $C_p = N/(n_x n_y)$ on the quality of the gradient statistics (i.e. the solution compared with
 416 the analytical solution and the standard deviation around the mean). As shown in [19], the
 417 particle size becomes a concern when it increases beyond a third of the size of the correlation
 418 window for the SRW. Here, we are not interested in the mean SRW but in the statistics of
 419 the derivatives. Hence, we analyse the standard deviation of the gradients at $y = 0$ for both
 420 OF and CC for particle sizes $d_\tau = [1, 2, 3, 4, 6]$ and particle concentrations $C_p = [0.049 -$
 421 $0.69]$ ppp.

422 Fig. 6(a) shows variations with respect to C_p while Fig. 6(b) reports variations with
 423 respect to the particle size d_τ , both for a displacement $\Delta x = 5$ px. For both cases, the standard
 424 deviation is nearly constant for OF while decreasing the interrogation window increases
 425 the standard deviation for CC. Also, decreasing the particle size and particle concentration
 426 degrades the quality of the reconstruction for CC while OF remains essentially insensitive
 427 to both parameters.

428 As a conclusion, OF provides greater robustness to parameter variations such as particle
 429 size and particle concentration, at least for the parameters investigated in this study, which
 430 are representative of many experiments, as will be shown in §5, and turbulent flow experi-
 431 ments in general.

432
 433 *As a rule of thumb:* OF appears to be more robust than CC when attempting to evaluate
 434 unresolved velocity gradients. As noted in the previous section, OF is slightly less precise
 435 when measuring mean displacements from particle images. The optimal value of KR ap-
 436 pears to be less dependent than CC when varying the particle size and particle concentration
 437 and is therefore strongly dependent on the physical scales of the flow. This will be demon-
 438 strated using turbulent measurements computed from both synthetic and real particle image
 439 turbulent experiments.

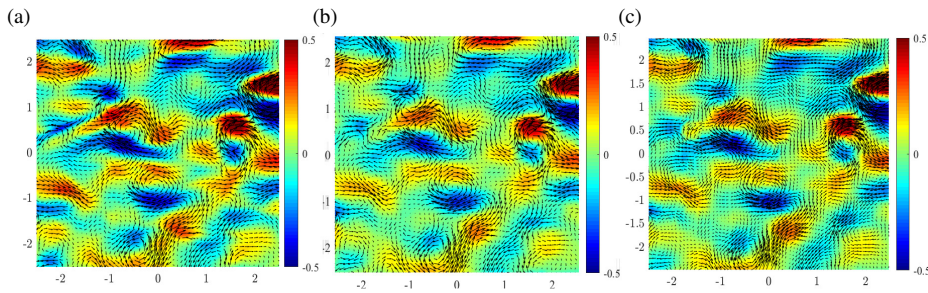


Fig. 7: Instantaneous velocity field results for the two-dimensional HITF dataset. DNS results (a), OF results (b), CC PIV results (c).

4 Two-dimensional turbulence data-set from synthetic particle images

The data-set used in the present study is available online and provided by [4]. It is the case of a forced time-resolved Homogeneous Isotropic Turbulent Flow (HITF) computed from a direct numerical simulation in two dimensions where particles are seeded without camera noise nor illumination variations. It corresponds to synthetic PIV images from the 4th PIV-Challenge [20]. In this data-set, the average particle radius is 2 px while the mean particle concentration is $C_p = 0.014$ ppp.

For DPIVsoft, an interrogation window of 16 and an overlap of 75% were used, which provided the best compromise between velocity calculation accuracy and spatial resolution. In the case of OF, several kernel radii were considered in order to investigate its influence on the quality of the reconstruction.

Snapshots of the velocity fields are shown in Fig. 7(a) for the DNS, Fig. 7(b) for OF and in Fig. 7(c) for CC. It is worth noting that the amplitudes are well measured by both PIV strategies but the border in OF shows a lack of resolution as particles may leave or enter through these boundaries. Furthermore, the gradients seem to be slightly smoothed for both OF and CC for this first visual inspection.

The data are also compared with the actual velocities from the DNS and the results are shown for the mean horizontal spectrum in Fig. 7(a) while the spectrum pre-multiplied by k^l (i.e. where $l = 2$ to show the dissipation spectrum) is shown in Fig. 7(b). Welch's method [46] was used for the calculation of the spectra, for which a Hamming window size equal to the full signal length was considered.

Note that here, we make the assumption of a two-dimensional isotropic and homogeneous flow which is shown to be the case in [4]. In addition, only 100 snapshots were available for the comparison for the DNS while 1000 PIV snapshots of particles are provided online but this was not an issue in order to compare the results and obtain conclusive remarks.

The present results show that decreasing the KR improves the quality of the velocity spectrum for OF (i.e. compared to the numerical simulation). In fact, the best results are obtained for $KR = 4$ for the largest to the smallest scales. Note that this KR is close to the size of the particles themselves; this will turn out to be the smallest size possible for all experiments and appears to be the minimum KR. The results for CC begin to depart from the DNS for $k \approx 1$ rad/px while the slope of the energy with respect to the wavenumber clearly departs for $k > 2.2$ rad/px and an exponent k^{-2} which is the point where the filtering effect induced by windowing was predicted. These estimates therefore remain robust, even for

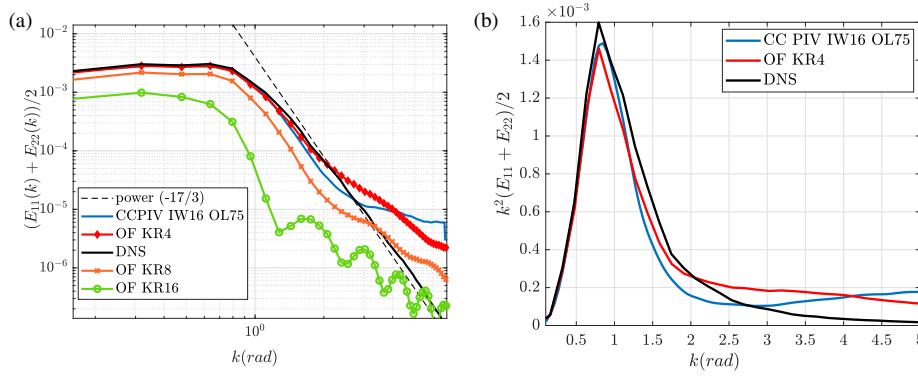


Fig. 8: (a) Velocity spectra comparison for the THIF data-set. Comparison with spectra from reference DNS data. 10 iterations and 2 pyramid levels are used for OF calculations. (b) Dissipation rate comparison for the THIF data-set. Comparison with spectra from reference DNS data.

474 complex flow fields (cf. Fig. 8(b)). In the case of OF, the departure between the two spectra
 475 appears at a lower wavenumber. In particular, the spectrum no longer displays a slope of
 476 $k^{-17/3}$ but a steeper exponent is found which is an interesting result in itself. This means
 477 that for synthetic data, the noise level is low enough so that OF is able to either smooth
 478 or capture accurate gradients, even for length scales where a spectrum close to k^{-6} . Note
 479 that the kinetic energy spectrum in two-dimensional turbulence follows a $k^{-5.7} \approx k^{-17/3}$
 480 spectrum for the enstrophy range, analogous to the dissipation range, as shown in [48]. This
 481 is also confirmed for the compensated spectrum shown in Fig. 8(b) where the compensated
 482 energy decreases with increasing k . Note that both CC and OF predict the peak of dissipation
 483 at $k = 0.8$ which is very close to the DNS.

484 This first analysis confirms that the KR necessary to achieve an accurate PIV calculation
 485 using OF is close to the particle size itself, which is 4 times smaller than the best window
 486 size achieved by CC. Note that here, the concentration is rather high while for the motion-
 487 less particle images, the concentration was nearly 2 times lower. Hence, it is important for
 488 an accurate OF reconstruction to ensure that particles are as small as possible and the con-
 489 centration as high as possible in order to accurately measure velocity gradients. This is not
 490 the case for CC, where individual particles must appear individually because of the FFT
 491 used for the correlation and the fact that several particles must be present in the IW. Note
 492 also that we performed CC using direct correlation and both method yield nearly identical
 493 results.

494 As a first rule of thumb, we can therefore see that the KR for OF has to be at least twice
 495 smaller than the interrogation window for CC in order to obtain comparable measurements.
 496 Furthermore, the optimal KR used in this benchmark was four times smaller than the interro-
 497 gation window size used in CC, which should lead to a twice more accurate result. However,
 498 the present test case makes it hard to confirm this assertion.

500 Next, we apply the same technique to real experimental snapshots, obtained in the case
 501 of a turbulent flow behind a regular grid and further demonstrate the robustness of OF com-
 502 pared to CC.

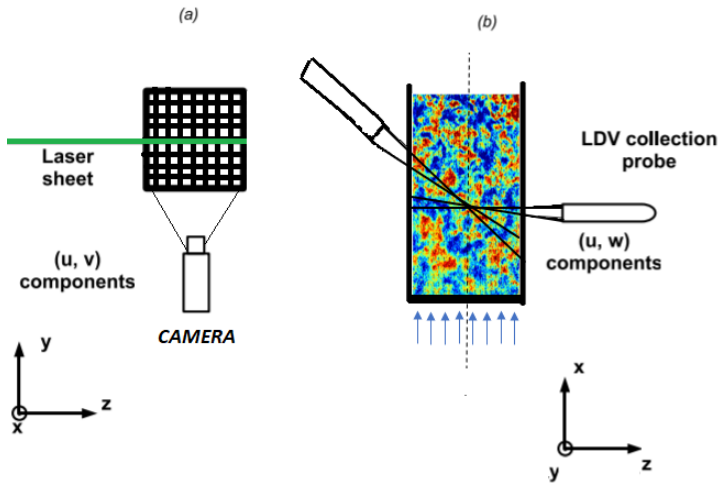


Fig. 9: Sketch of the grid turbulence experiment showing the PIV plane and the LDV measurement probes. Only the u component from LDV measurements is considered.

503 5 Experimental results

504 First it should be noted that the velocity fields presented in the following are obtained with-
505 out pre-processing or filtering of the raw particle images.

506 5.1 Grid turbulence experiment

507 The experimental grid turbulence dataset was first presented in [25] to improve premixed
508 combustion. The energy transfer through turbulent scales was analysed through a close in-
509 spection of the scale-by-scale energy transport equation based on Laser-Doppler Velocime-
510 try (LDV). Experiments were carried out in an open-loop vertical wind tunnel [25]. The
511 wind-tunnel cross-section was $8 \times 8 \text{ cm}^2$. The test-section was 40 cm long and allowed easy
512 optical access. The turbulence intensity was 0.4 % and the inlet free-stream velocity was
513 $U = 3.7 \text{ m.s}^{-1}$. In the present work, the analysis is restricted to the turbulent flow generated
514 by a single perforated plate [25] (i.e. the intermediate grid of the MuSTI turbulence genera-
515 tor). This plate consists of a mesh of circular holes of 6 mm diameter each, that spans over
516 the entire wind tunnel. The holes are arranged in a triangular network with a 9 mm spacing.
517 Moreover, the perforation is straight over the entire thickness of the plates and the holes
518 network is chosen such that the tunnel's centre line coincide with a hole centre.

519 The flow was illuminated by an Nd-Yag laser (Big Sky laser, 120 mJ/pulse, 532 nm).
520 The laser sheet coincides with the vertical mid-plane of the test section corresponding to
521 the (x, z) -plane (see Fig. 9). The wind-tunnel was seeded with olive oil droplets generated
522 and injected far upstream the test section. The average diameter d_τ of the olive oil particles
523 is close to $1 \mu\text{m}$ and the resulting Stokes number is much lower than 0.1 ensuring a good
524 flow tracing [25]. The snapshots were acquired using a CCD camera (FlowMaster LaVision,
525 12-bits, $1280 \times 1024 \text{ px}^2$) with a 50 mm $f/1.2$ Nikkor lens. The magnification ratio is of
526 16 px/mm, leading to a field of view of $80 \text{ mm} \times 64 \text{ mm}$.

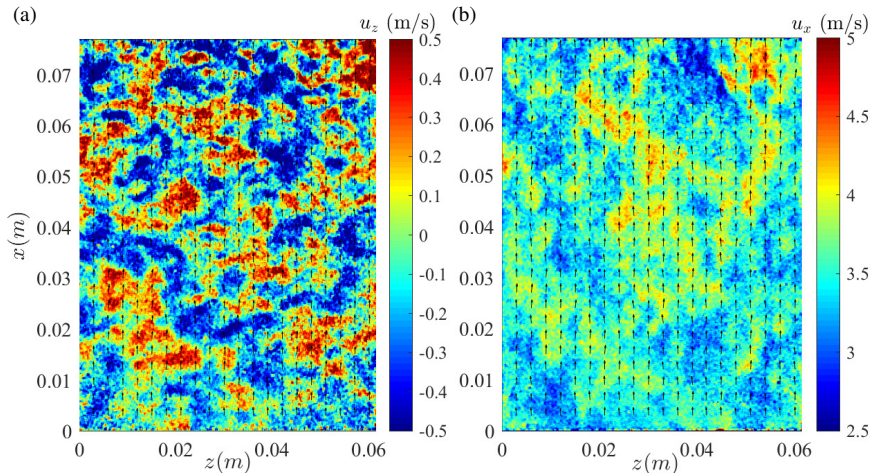


Fig. 10: Illustration of instantaneous spanwise (a) and streamwise (b) velocity fields of the wind tunnel grid turbulence experiment, computed using OF with $KR = 8$.

527 The dataset consists of 1600 snapshots. An Example of an instantaneous spanwise and
 528 streamwise velocity components computed with OF are shown in Fig. 10 (a) and (b) respec-
 529 tively. In this dataset, the average particle diameter is $d_\tau = 3.5$ px, while the mean particle
 530 concentration is $C_p = 0.014$ ppp.

531 This canonical flow, which is nearly homogeneous and isotropic turbulence, provides an
 532 ideal case to assess the filtering effect of both PIV methods (i.e. CC and OF). To this end,
 533 a scale-by-scale analysis of the turbulent kinetic energy is carried out in the following. This
 534 analysis will be compared to LDV measurements performed at the centre of the image, in
 535 the mid-channel plane as shown in Fig. 9. First, we introduce the velocity increment $\Delta u_i(\mathbf{r})$
 536 such that:

537

$$\Delta u_i(\mathbf{r}) = u_i(\mathbf{x} + \mathbf{r}) - u_i(\mathbf{r}) \quad (7)$$

538 where i designates any velocity component and r stands for the separation length vector. Un-
 539 der the isotropy hypothesis, the second-order structure function $S_{2q} = \Delta q^2(\mathbf{r}) \equiv (\Delta u_i)^2(\mathbf{r})$
 540 only depends on r , the modulus of the separation \mathbf{r} , and represents the total kinetic energy
 541 of the scale r . It is worth noting that unlike LDV measurements which restrict scale-by-
 542 scale analyses to a single direction, that is $\mathbf{r} = r\mathbf{e}_x$, using Taylor's hypothesis, PIV mea-
 543 surements obtained by both CC and OF allow for computing increments along both $r\mathbf{e}_x$ and
 544 $r\mathbf{e}_z$. However, for spatially decaying turbulence, the streamwise direction is subject to non-
 545 homogeneous effects and analyses were therefore restricted to the flow-normal direction \mathbf{e}_z ,
 546 for comparison with LDV measurements.

547 The second-order structure function calculated for both CC and OF are shown in Fig. 11(a)
 548 and Fig. 11(b) respectively. In principle, the structure function should scale with the separa-
 549 tion distance as $r^{2/3}$ in the inertial range and as r^2 in the viscous range [42], as shown
 550 in both figures. In addition, the Taylor microscale λ is also shown while the Kolmogorov
 551 microscale η is too small to be reported in the figures. Note that the $r^{2/3}$ scaling, associated
 552 with the turbulent cascade, is difficult to distinguish since the Taylor Reynolds number is
 553 small (i.e. $Re_\lambda \approx 45$). Both scales were computed using $\eta \equiv (v^3/\varepsilon)^{1/4} \approx 6 \times 10^{-5}$ m and

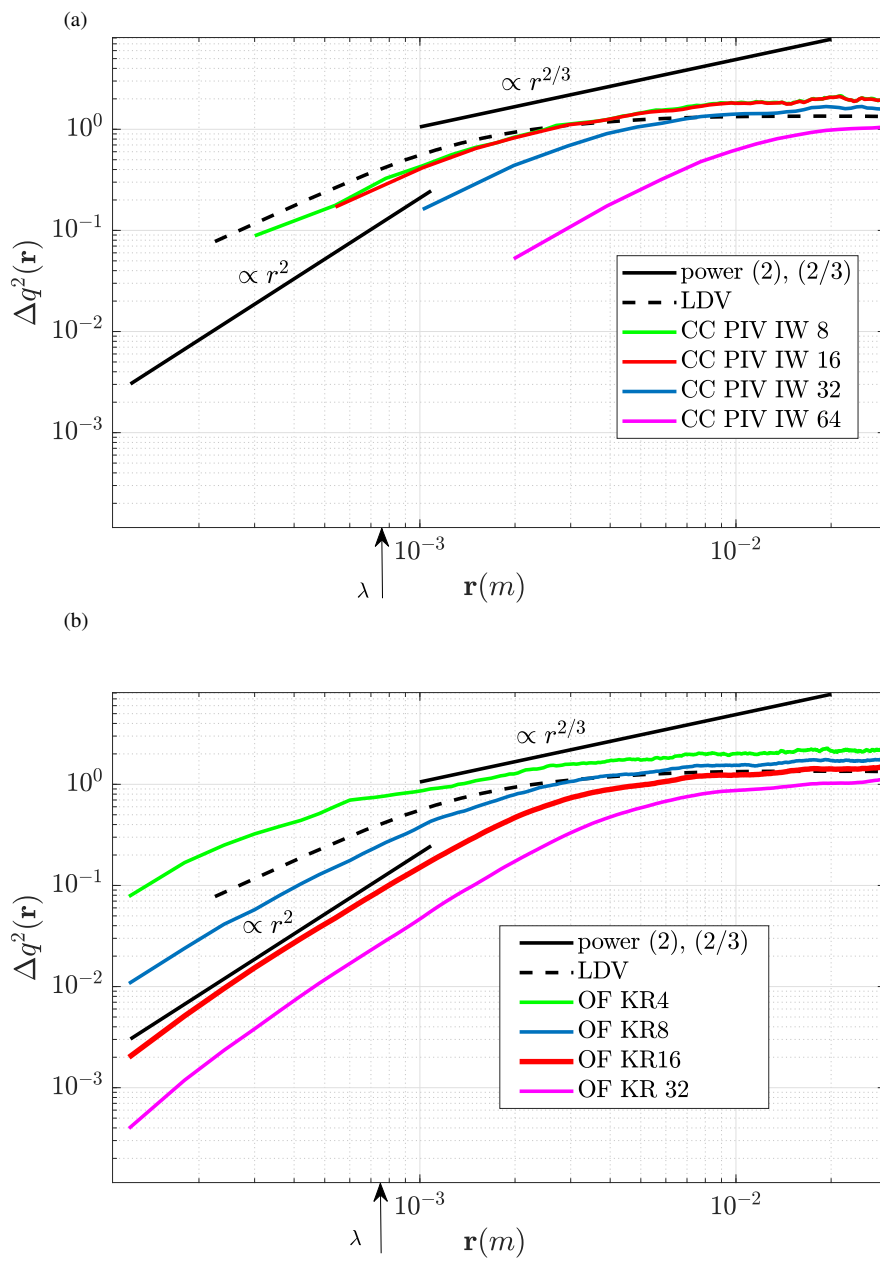


Fig. 11: Evolution of the second-order structure function with respect to the separation scale r along the normal direction to the mean flow, for CC PIV (a), OF (b) compared to LDV measurements. Results are averaged in time.

554 $\lambda = \sqrt{5\nu q^2/\varepsilon_h} \approx 7.4 \times 10^{-4}$ m, with ε_h defined as:

$$\varepsilon_h = 3\nu \left[\left\langle \left(\frac{\partial u}{\partial x} \right)^2 \right\rangle + \left\langle \left(\frac{\partial v}{\partial x} \right)^2 \right\rangle + \left\langle \left(\frac{\partial w}{\partial x} \right)^2 \right\rangle \right]. \quad (8)$$

555 where $\langle \cdot \rangle$ denotes the averaging operator and ε_h is computed using LDV measurements.

556 First, we analyse the filtering effect of CC and OF in Fig. 11(a,b). As noted before,
557 the large scales are essentially independent of the window size used for CC (i.e. except for
558 $X = 64$ px) while the spread induced by the smoothing of OF is more pronounced. Once
559 again, the kernel radius used for OF has to be twice larger than the window size used for CC
560 to obtain similar results.

561 Further inspecting the large scales, $S_{2q}(r)$ appears to be dependent on the size of IW
562 and KR. This is not surprising since for this configuration, the large scales (i.e. the integral
563 lengthscale $\Lambda \approx 50$ px ≈ 3 mm). Therefore, interrogation windows or kernel radii larger than
564 $\lambda \times 2.8/2\pi \approx 22$ px will not be able to capture the asymptotic value of $\Delta q^2(\mathbf{r})$ for $\mathbf{r} \gg \Lambda$.
565 This observation is verified for CC in Fig. 11(a) where the structure function converges as
566 the interrogation window size IW decreases. This result is however not true for OF and the
567 asymptotic value $\Delta q^2(\mathbf{r})$ for the larger values of \mathbf{r} as shown in Fig. 11(b). At this point, it is
568 necessary to analyse the spectra to determine why this effect occurs.

569 The spectra of the streamwise component were calculated on the streamwise profile
570 along the x axis in the middle of the snapshots ($z = 0.03$ mm) and compared with spectra
571 from the LDV probe. Welch's method [46] was again used for the calculation of the spectra,
572 for which a Hamming window size equal to the full signal length was consistently chosen.
573 It is worth mentioning that unlike for the structure function, a direct comparison between
574 LDV and PIV spectra is not obvious due to longitudinal inhomogeneities in the flow.

575 The spectra obtained for various KR and IW size are presented in Fig. 12. Interestingly,
576 the results are quite similar when the IW of CC is equal to twice the KR of OF. Nonetheless,
577 only OF with $KR = 8$ follows the LDV measurements up to $k = 5000$ (rad/m) and the onset
578 of the Taylor subrange. On the other hand, the optimal IW for CC-PIV was $X = 16$ which is
579 in line with the structure function analysis. The maximum wavelength with good agreement
580 compared to the LDV measurements is around $k = 2000$ (rad/m). In this test case, CC is
581 not able to capture the Taylor micro scale while OF can achieve this measurement. This is
582 also visible in the structure function in Fig. 11(b) where the \mathbf{r}^2 scaling associated with the
583 diffusive range is clearly visible for $KR = 8$.

584 The spectra shown in Fig. 12 explain why structure functions computed with OF do not
585 converge at large separation distances \mathbf{r} . Spectra computed with CC appear to be essentially
586 independent of the interrogation window size $IW = 16$ and $IW = 8$ for $k > 10^3$ (i.e. they
587 overlap). At the contrary, spectra computed with OF and $KR = 8$ and $KR = 4$ separate
588 significantly for $k > 1000$ (rad/m). Getting back to the definition of the structure function
589 $S_{2q}(\mathbf{r}) = \Delta q^2(\mathbf{r}) = \langle (q(\mathbf{r} + \Delta \mathbf{r}) - q(\mathbf{r}))^2 \rangle$, and looking at large separation distances $r \gg \Lambda$,
590 the structure function $S_{2q}(\mathbf{r}) \approx 2\langle q(\mathbf{r})^2 \rangle$ is only dependent on the Turbulent Kinetic Energy
591 (TKE). However, integrating both OF spectra (i.e. computing the TKE) for $KR = 8$ and
592 $KR = 4$ leads to different values (i.e. because of the energy increase for $k > 2000$) which
593 correspond to the differences observed in Fig. 11(b) at large separation distances \mathbf{r} .

594 For scales close to the Taylor microscale λ , the results for the structure function com-
595 puted with CC are consistent for window sizes of 8 and 16 px. For larger window sizes, the
596 estimation of the structure function falls below the estimate of LDV measurements. The re-
597 sults obtained with optical flow is somewhat different. The structure function $S_{2q}(\mathbf{r})$ appears
598 to be strongly dependent on the size of the KR used for the analysis, which is different than

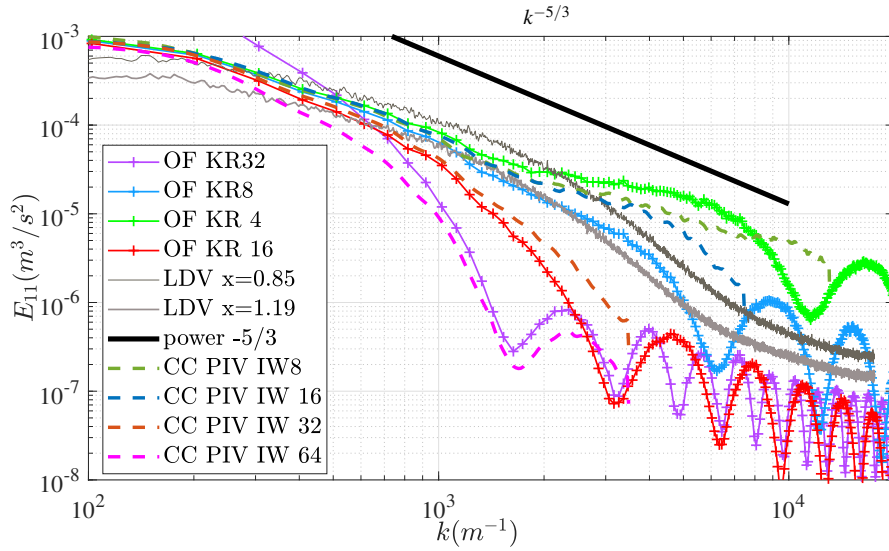


Fig. 12: Time-averaged velocity spectra of the streamwise velocity component along a streamwise profile in the centre of the velocity field, compared with LDV measurements spectra at two streamwise positions ($z = 0.02$ and $x = 0.06$ shown in Fig. 10).

599 for CC. In particular, the best fit is obtained with $KR = 8$ which follows both LDV mea-
 600 surements and the best results obtained using CC. The smoothing induced by OF becomes
 601 even more visible at $S_{2q}(\mathbf{r} \approx \lambda \approx KR)$ where the diffusion induced by OF follows the \mathbf{r}^2
 602 scaling for all cases. This particular effect is reminiscent of the smoothing induced by the
 603 sub-grid resolution which is clearly of diffusive type and therefore well suited for turbulent
 604 flows when the Taylor microscale can be resolved.

605 For $\mathbf{r} < \lambda$, the subgrid resolution obtained with OF is found to scale with \mathbf{r}^2 which
 606 can be seen as the diffusion induced by OF for sub-kernel estimations of the velocity. This
 607 particular feature further supports the idea that for distances smaller than the size of the
 608 kernel radius ($\mathbf{r} < KR$), OF acts as a diffusion process while, for $KR \approx \lambda$, subpixel velocity
 609 calculations may represent an interesting alternative to estimate subgrid velocities.

610 *As a rule of thumb:* The best compromise for CC appears to be correlation boxes with
 611 $X = Y = 16$ as already noticed in [9]. However, OF provides an alternative. When the kernel
 612 radius approaches the Taylor microscale, that is $KR \approx \lambda$ and $KR8$, the method is able to
 613 accurately resolve the scales larger than the Taylor microscale and provides a sub-kernel
 614 approximation for $r < \lambda$ which scales as r^2 , equivalent to the diffusion-type effect identified
 615 in the previous sections of this study. This effect confirms the original idea of [40] that OF
 616 can be used for scales smaller than the ones provided by CC. However, it is important to
 617 stress that OF can be strongly dependent on KR and that the later has to be well tuned for
 618 turbulent flows in order to obtain accurate results.

6 Conclusion

A comparison between Optical Flow and Cross-Correlation PIV is undertaken in order to understand the advantages of each algorithms for turbulent flow applications. The performances of OF and CC-PIV have been evaluated on various test cases, from still flow, step displacement of synthetic images, 2D isotropic turbulence and finally experimental images from a grid-generated turbulence.

No-motion velocity fields show that OF and CC provide the same results in terms of noise and transfer function guided by the window size, as shown in Foucault *et al.* [8]. CC provides a lower noise level than OF and a higher frequency cut-off for the gradient. Analysing the step-response, OF is shown to be less accurate and more diffusive, but the gradients ($std(dU/dy)$) are better resolved with OF where the noise level is twice lower than for CC). Step-motion test showed that CC and OF behave differently when varying KR and IW compared with the effective particle size d_τ and the particle concentration C_p . OF appears more consistent, keeping lower errors for a wider range of image parameters.

Application to HIT from synthetic images confirms the same trend: OF is more diffusive but more accurate in computing the turbulent spectrum. The grid turbulence experimental dataset showed the same trend down to the Taylor micro-scale: OF is more diffusive but lower KR allows for resolving nearly the entire range of scales. However, accuracy is dependent on the value of KR and the later needs to be finely tuned in order to obtain well-converged results.

To summarise, the best compromise for CC remains $X = Y \lesssim 32$ with an overlap of 50%. For OF, similar results are obtained when $KR \approx X/2$ but OF is less sensitive to unresolved velocity gradients which is of paramount importance in turbulent flow analysis. The sub-kernel radius values undergo a heat-diffusion-type diffusion which prevents unresolved velocity gradients to propagate correlation errors but for $KR > 4$. Such a measurement might prove of interest when the Taylor microscale can be resolved, that is when the value of KR can be set close or smaller than the Taylor microscale.

Considering the present test cases, we can conclude that CC can be more precise than OF based on pure velocity calculations. However, OF's diffusion decreases the variance of the velocity gradients. This proves to be a critical advantage when PIV is applied to experimental turbulent flows, with windows nearly the size of the particles. OF is therefore more relevant to study such flows when the camera sensor is able to resolve enough particles and achieve resolution down to the Taylor micro-scale. This result therefore opens new alleys to study the effect of small-scale turbulence in turbulent flows. Nevertheless, there remains open questions when comparing OF and CC regarding turbulent flows. Comparing the role of the displacement on the quality of the reconstruction, time-resolved data and the computational time could further help understanding the benefit of each method.

Acknowledgements:

A. G. and J.-L. A. acknowledge the support by ANRT and Photon Lines. P.-Y. P. and N. M. acknowledge the support by the Agence Nationale de la Recherche (ANR) through the Investissements d'Avenir program under the Labex CAPRYSSSES Project (ANR-11-LABX-0006-01), the project APR IA PRESERVE, Région Centre-Val-de-Loire (2019 134933), and the project APR IA APROPORE, Région Centre-Val-de-Loire (2017 119967). Authors would also like to thank the anonymous referee who helped improving the overall quality of the paper.

664 Declaration of interest:

665 The doctoral thesis of the author A. Giannopoulos was funded by Photon Lines.

666 References

- 667 1. E. Adelson, C. Anderson, J. Bergen, P. Burt, and J. Ogden. Pyramid methods in image processing. *RCA*
668 *Eng.*, 29, 11 1983.
- 669 2. S. Cai, J. Liang, Q. Gao, C. Xu, and R. Wei. Particle image velocimetry based on a deep learning motion
670 estimator. *IEEE Transactions on Instrumentation and Measurement*, 69(6):3538–3554, 2020.
- 671 3. R. Camassa, M. W. Hurley, R. M. McLaughlin, P.-Y. Passaggia, and C. F. Thomson. Experimental
672 investigation of nonlinear internal waves in deep water with miscible fluids. *J. Ocean Eng. and Marine*
673 *Ener.*, 4(4):243–257, 2018.
- 674 4. J. Carlier. Second set of fluid mechanics image sequences. in: European project 'fluid image analysis
675 and description, fluid (2005).. *FLUID*, 2005.
- 676 5. F. Champagnat, A. Plyer, G. Le Besnerais, B. Leclaire, S. Davoust, and Y. Le Saint. Fast and accurate PIV
677 computation using highly parallel iterative correlation maximization. *Experiments in Fluids*, 50:1169–
678 1182, 2011.
- 679 6. S. Davoust, L. Jacquin, and B. Leclaire. Dynamics of $m = 0$ and $m = 1$ modes and of streamwise vortices
680 in a turbulent axisymmetric mixing layer. *Journal of Fluid Mechanics*, 709:408–444, 2012.
- 681 7. A. Dosovitskiy, P. Fischer, E. Ilg, P. Häusser, C. Hazirbas, V. Golkov, P. v. d. Smagt, D. Cremers, and
682 T. Brox. FlowNet: Learning optical flow with convolutional networks. In *2015 IEEE International*
683 *Conference on Computer Vision (ICCV)*, pages 2758–2766, 2015.
- 684 8. J.-M. Foucaut, J. Carlier, and M. Stanislas. Piv optimization for the study of turbulent flow using spectral
685 analysis. *Measurement Science and Technology*, 15(6):1046, 2004.
- 686 9. J.-M. Foucaut and M. Stanislas. Some considerations on the accuracy and frequency response of some
687 derivative filters applied to particle image velocimetry vector fields. *Meas. Sci. Tech.*, 13(7):1058, 2002.
- 688 10. N. Gautier. Flow control using optical sensors. *Ph. D thesis*, 2014.
- 689 11. N. Gautier and J.-L. Aider. Control of the separated flow downstream of a backward-facing step using
690 visual feedback. *Proceedings of the Royal Society A: Mathematical, Physical and Engineering Sciences*,
691 469(2160):20130404, 2013.
- 692 12. N. Gautier and J.-L. Aider. Frequency-lock reactive control of a separated flow enabled by visual sensors.
693 *Experiments in Fluids*, 56(1):16, Jan 2015.
- 694 13. N. Gautier and J.-L. Aider. Real-time planar flow velocity measurements using an optical flow algorithm
695 implemented on gpu. *Journal of Visualization*, 18(2):277–286, 2015.
- 696 14. N. Gautier, J.-L. Aider, T. Duriez, B. Noack, M. Segond, and M. Agel. Closed-loop separation control
697 using machine learning. *J.Fluid.Mech.*, 770:442–457, 2015.
- 698 15. W. K. George and M. Stanislas. On the noise in statistics of piv measurements, 2020.
- 699 16. A. Giannopoulos and J.-L. Aider. Data-driven order reduction and velocity field reconstruction using
700 neural networks: The case of a turbulent boundary layer. *Physics of Fluids*, 32(9):095117, 2020.
- 701 17. A. Giannopoulos and J.-L. Aider. Prediction of the dynamics of a backward-facing step flow using
702 focused time-delay neural networks and particle image velocimetry data-sets. *International Journal of*
703 *Heat and Fluid Flow*, 82:108533, 2020.
- 704 18. B. K. Horn and B. G. Shunck. Determining optical flow. *Artificial Intelligence*, 17:185–203, 08 1981.
- 705 19. C. J. Kähler, S. Scharnowski, and C. Cierpka. On the resolution limit of digital particle image velocime-
706 try. *Experiments in fluids*, 52(6):1629–1639, 2012.
- 707 20. C. J. Kähler, P. P. Astarita, Tommaso and Vlachos, J. Sakakibara, R. Hain, S. Discetti, R. La Foy, and
708 C. Cierpka. Main results of the fourth international piv challenge. *Experiments in Fluids*, 57, 2016.
- 709 21. T. Liu, A. Merat, H. Makhmalbaf, C. Fajardo, and P. Merati. Comparison between optical flow and
710 cross-correlation methods for extraction of velocity fields from particle images. *Experiments in Fluids*,
711 56:166, 08 2015.
- 712 22. T. Liu, A. Merat, M. H. M. Makhmalbaf, and C. a. Fajardo. Comparison between optical flow and cross-
713 correlation methods for extraction of velocity fields from particle images. *Experiments in Fluids*, 56,
714 2015.
- 715 23. T. Liu, D. M. Salazar, H. Fagehi, H. Ghazwani, J. Montefort, and P. Merati. Hybrid Optical-Flow-Cross-
716 Correlation Method for Particle Image Velocimetry. *Journal of Fluids Engineering*, 142(5), 02 2020.
717 054501.

- 718 24. L. Lourenco. True resolution piv: a mesh-free second order accurate algorithm. In *10th Int. Symp. on*
719 *Applications of Laser Techniques in Fluid Mechanics (Lisbon), 2000, 2000.*
- 720 25. N. Mazellier, L. Danaïla, and B. Renou. Multi-scale energy injection: a new tool to generate intense
721 homogeneous and isotropic turbulence for premixed combustion. *J. Turb.*, 11:N43, 2010.
- 722 26. L. Mendes, A. Bernardino, and R. M. Ferreira. Piv-image-generator: An image generating software
723 package for planar piv and optical flow benchmarking. *SoftwareX*, 12:100537, 2020.
- 724 27. P. Meunier and T. Leweke. Analysis and treatment of errors due to high velocity gradients in particle
725 image velocimetry. *Exp. Fluids*, 35(5):408–421, 2003.
- 726 28. C. Pan, X. Dong, X. Yang, W. Jinjun, and W. Runjie. Evaluating the accuracy performance of lucas-
727 kanade algorithm in the circumstance of piv application. *Sci. China-Phys. Mech. Astron.*, 58, 2015.
- 728 29. P.-Y. Passaggia, V. K. Chalamalla, M. W. Hurley, A. Scotti, and E. Santilli. Estimating pressure and
729 internal-wave flux from laboratory experiments in focusing internal waves. *Experiments in Fluids*,
730 61(11):1–29, 2020.
- 731 30. P.-Y. Passaggia, T. Leweke, and U. Ehrenstein. Transverse instability and low-frequency flapping in
732 incompressible separated boundary layer flows: an experimental study. *Journal of fluid mechanics*,
733 703:363, 2012.
- 734 31. G. Quénot, J. Pakleza, and T. Kowalewski. Particle Image Velocimetry with Optical Flow. *Experiments*
735 *in Fluids*, 25(3):177–189, 1998.
- 736 32. J. Rabault, J. Kolaas, and A. Jensen. Performing particle image velocimetry using artificial neural net-
737 works: a proof-of-concept. *Measurement Science and Technology*, 28(12):125301, nov 2017.
- 738 33. M. Raffel, C. E. Willert, J. Kompenhans, et al. *Particle image velocimetry: a practical guide*, volume 2.
739 Springer, 1998.
- 740 34. P. Ruhnau, T. Kohlberger, C. Schnörr, and H. Nobach. Variational optical flow estimation for particle
741 image velocimetry. *Exp. Fluids*, 38:21–32, 01 2005.
- 742 35. F. Sartor, G. Losfeld, and R. Bur. Piv study on a shock-induced separation in a transonic flow. *Experi-*
743 *ments in Fluids*, 53:815–827, 9 2012.
- 744 36. F. Scarano and M. Riethmuller. Advances in iterative multigrid piv image processing. *Exp. Fluids*,
745 29:S051–S060, 04 2012.
- 746 37. B. Schmidt and J. Sutton. Improvements in the accuracy of wavelet-based optical flow velocimetry
747 (wofv) using an efficient and physically based implementation of velocity regularisation. *Exp. Fluids*,
748 61, 01 2020.
- 749 38. B. E. Schmidt and J. A. Sutton. High-resolution velocimetry from tracer particle fields using a wavelet-
750 based optical flow method. *Exp. Fluids*, 60(3):37, 2019.
- 751 39. A. Sciacchitano, B. Wieneke, and F. Scarano. Piv uncertainty quantification by image matching. *Mea-*
752 *surement Science and Technology*, 24:045302, 03 2013.
- 753 40. j. h. Seong, M. Song, D. Núñez, A. Manera, and E. Kim. Velocity refinement of piv using global optical
754 flow. *Exp. Fluids*, 60, 10 2019.
- 755 41. R. Shanmughan, P.-Y. Passaggia, N. Mazellier, and A. Kourta. Optimal pressure reconstruction based on
756 planar particle image velocimetry and sparse sensor measurements. *Exp. Fluids*, 61(11):1–19, 2020.
- 757 42. Z.-S. She and E. Leveque. Universal scaling laws in fully developed turbulence. *Phys. Rev. Lett.*,
758 72(3):336, 1994.
- 759 43. M. Stanislas, K. Okamoto, and C. K. hler. Main results of theFirst international PIV challenge. *Mea-*
760 *surement Science and Technology*, 14(10):R63–R89, sep 2003.
- 761 44. M. Stanislas, K. Okamoto, C. J. Kähler, and J. Westerweel. Main results of the second international piv
762 challenge. *Experiments in Fluids*, 39:170–191, 2005.
- 763 45. M. Stanislas, K. Okamoto, C. J. Kähler, J. Westerweel, and F. Scarano. Main results of the third interna-
764 tional piv challenge. *Experiments in Fluids*, 45:27–71, 2008.
- 765 46. P. Stoica and R. Moses. Spectral analysis of signals. *Prentice Hall*, 01 2005.
- 766 47. W. Thielicke and E. J. Stamhuis. PIVlab – towards user-friendly, affordable and accurate digital particle
767 image velocimetry in MATLAB. *Journal of Open Research Software*, 2, oct 2014.
- 768 48. C. V. Tran and J. C. Bowman. Robustness of the inverse cascade in two-dimensional turbulence. *Phy.*
769 *Rev. E*, 69(3):036303, 2004.
- 770 49. E. Varon, J.-L. Aider, Y. Eulalie, S. Edwige, and P. Gilotte. Adaptive control of the dynamics of a fully
771 turbulent bimodal wake using real-time piv. *Exp. Fluids*, 60(8):124, 2019.
- 772 50. E. Varon, Y. Eulalie, S. Edwige, P. Gilotte, and J.-L. Aider. Chaotic dynamics of large-scale structures
773 in a turbulent wake. *Phys. Rev. Fluids*, 2:034604, Mar 2017.
- 774 51. D. Vig, A. Hamby, and C. Wolgemuth. On the quantification of cellular velocity fields. *Biophysical*
775 *Journal*, 110(7):1469 – 1475, 2016.
- 776 52. H. Wang, G. He, and S. Wang. Globally optimized cross-correlation for particle image velocimetry. *Exp.*
777 *Fluids*, 61, 10 2020.
- 778 53. J. Westerweel. *Digital Particle Image Velocimetry - Theory and Application*. Delft University Press,
779 1993.